

InFusionSurf: Refining Neural RGB-D Surface Reconstruction Using Per-Frame Intrinsic Refinement and TSDF Fusion Prior Learning

Seunghwan Lee, Gwanmo Park, Hyewon Son, Jiwon Ryu, Han Joo Chae

ROKIT Healthcare, Inc.

{seunghwan.lee, gwanmo.park, hyewon.son, jiwon.ryu, hanjoo.chae}@rokit.co.kr

Abstract

We introduce InFusionSurf, a novel approach to enhance the fidelity of neural radiance field (NeRF) frameworks for 3D surface reconstruction using RGB-D video frames. Building upon previous methods that have employed feature encoding to improve optimization speed, we further improve the reconstruction quality with minimal impact on optimization time by refining depth information. Our per-frame intrinsic refinement scheme addresses frame-specific blurs caused by camera motion in each depth frame. Furthermore, InFusionSurf utilizes a classical real-time 3D surface reconstruction method, the truncated signed distance field (TSDF) Fusion, as prior knowledge to pretrain the feature grid to support reconstruction details while accelerating the training. The quantitative and qualitative experiments comparing the performances of InFusionSurf against prior work indicate that our method is capable of accurately reconstructing a scene without sacrificing optimization speed. We also demonstrate the effectiveness of our per-frame intrinsic refinement and TSDF Fusion prior learning techniques via an ablation study.

Introduction

A neural RGB-D surface reconstruction method (Azinović et al. 2022) recently incorporated a depth-measurement-based implicit surface representation into the volume rendering scheme of neural radiance field (NeRF) (Mildenhall et al. 2020) and achieved high-quality geometry estimates of entire scenes. However, similar to most NeRF variants, Neural RGB-D (Azinović et al. 2022) requires a long optimization time for each new scene; the study reports to take 9 to 13 hours, depending on the size of the scene. While fast and precise 3D surface reconstruction is necessary for many real-world applications, various methods have attempted to address the convergence speed through the adoption of explicit representations. (Sun, Sun, and Chen 2021; Müller et al. 2022; Takikawa et al. 2021; Wang, Bleja, and Agapito 2022; Sun et al. 2021).

Furthermore, commercial image-capturing devices can introduce inherent distortions, such as motions blurs, defocus blurs, and rolling shutter effects, to video frames, degrading scene reconstruction quality. Most variants of NeRF methods struggle to reconstruct sharp images from blurry inputs. While a few NeRF-integrated deblurring schemes (Ma et al. 2022) have been introduced to correct distortions in

the color frames, they only have limited effects on the quality when it comes to the depth-dependent 3D reconstruction. Camera motion blurs in depth frames exhibit distinct characteristics from color frames and have a more significant impact on the results.

In this work, we propose *InFusionSurf*¹, a NeRF-style RGB-D 3D surface reconstruction framework that refines depth information to enhance reconstruction quality with minimal impact on optimization time. The base structure of InFusionSurf utilizes a dense feature grid and shallow multi-layer perceptrons (MLP) and our novel depth-specific schemes further enhance the accuracy of the reconstruction for the entire scene. Our per-frame intrinsic refinement scheme introduces explicit parameters to optimize the rendering ray directions to handle the camera motion blurs in RGB-D videos with only a marginal effect on the training speed. Furthermore, InFusionSurf utilizes a classical real-time 3D surface reconstruction method with depth frames (i.e., the truncated signed distance field (TSDF) Fusion (Curless and Levoy 1996)) as prior knowledge to pretrain the feature grid to support the model to concentrate on the fine details during subsequent training phases. By comparing the performance against prior work (i.e., Neural RGB-D (Azinović et al. 2022) and GO-Surf (Wang, Bleja, and Agapito 2022)), we show how InFusionSurf accurately reconstructs a scene without sacrificing optimization speed. Moreover, we demonstrate the effectiveness of the TSDF Fusion prior learning and per-frame intrinsic refinement techniques via an ablation study.

Related work

Our method focuses on reconstructing 3D scenes from a sequence of RGB-D frames and relates to previous works on TSDF-based 3D reconstruction, coordinate-based implicit neural representations, and image deblurring methods.

Classical 3D reconstruction

Variants of TSDF Fusion method (Curless and Levoy 1996) have been commonly used for reconstructing 3D surfaces from depth images (Zollhöfer et al. 2018). Numerous improvements, such as real-time applications (Newcombe et al. 2011), spatial hashing for efficient memory usage (Nießner

¹<https://rokit-healthcare.github.io/InFusionSurf>

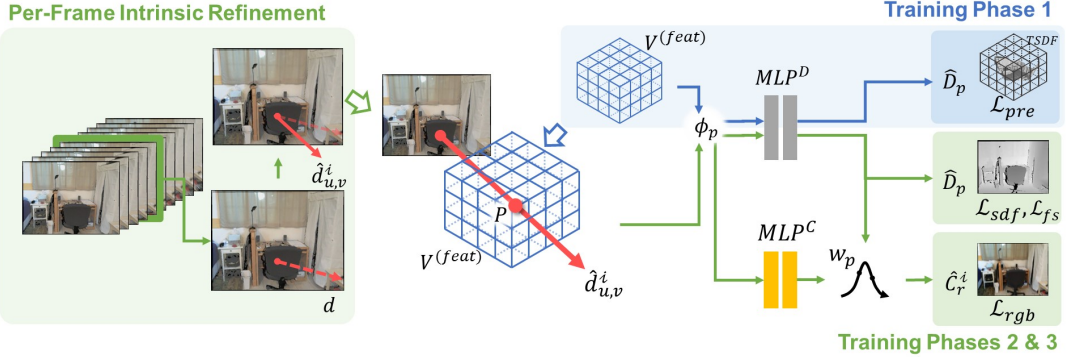


Figure 1: Our method proposes per-frame intrinsic refinement and classical TSDF Fusion prior learning schemes for high-quality 3D surface reconstruction with minimal impact on optimization time. We adopt the Neural RGB-D method, revised with a dense feature grid and shallow MLPs. Our per-frame intrinsic refinement scheme compensates for the frame-specific distortion effects caused by the camera motion. The first phase of the training learns geometric prior using the TSDF Fusion algorithm and the later phases adopt a progressive learning technique.

et al. 2013), and better reconstruction quality through camera pose estimation (Dai et al. 2016), have been implemented over the years.

While TSDF Fusion-based methods are fast and efficient, they often exhibit limitations, such as holes or geometric artifacts in the reconstruction results. Nevertheless, we found that using TSDF Fusion output as the target while pretraining our voxel feature grid and MLPs improves the reconstruction quality while accelerating the convergence speed.

Neural radiance field and depth

Various attempts have been made to adapt the neural radiance field representation and volume rendering scheme (Mildenhall et al. 2020) to depth images. Some methods incorporated depth priors for better novel view synthesis (Chen et al. 2021; Wei et al. 2021; Deng et al. 2021; Neff et al. 2021), while others used implicit neural representations for 3D surface reconstruction (Wang et al. 2021; Yariv et al. 2020; Oechsle, Peng, and Geiger 2021; Sucar et al. 2021; Ortiz et al. 2022; Peng et al. 2020; Chen and Zhang 2018).

Given the long optimization time of NeRF and its variants, methods for quicker convergence have been proposed (Sun, Sun, and Chen 2021; Müller et al. 2022; Takikawa et al. 2021; Sun et al. 2021). GO-Surf (Wang, Bleja, and Agapito 2022) combines a multi-resolution feature grid with a hybrid volume rendering scheme akin to Neural RGB-D for faster optimization speed.

Our approach adopts Neural RGB-D (Azinović et al. 2022) and a dense feature grid representation to achieve accurate and accelerated 3D scene reconstruction. We further introduce the per-frame intrinsic refinement scheme and a TSDF Fusion-guided pretraining phase to enhance reconstruction quality, outperforming GO-Surf and Neural RGB-D in quality without sacrificing optimization speed.

Camera motion blur handling

Numerous methods for color image deblurring have been proposed (Wang and Tao 2014), including those based on convolutional neural networks (Nah, Kim, and Lee 2018; Tao et al. 2018; Zamir et al. 2021) or generative models (Kupyn et al. 2018, 2019). Deblur-NeRF (Ma et al. 2022) integrated the blurring process into NeRF, employing deformable kernels to restore sharp color images from blurry inputs.

To effectively address depth-specific motion blurs, we employ the per-frame intrinsic refinement technique for optimizing rendering ray directions. This involves constrained deformable kernels that apply translation and scaling transformations across the entire image planes (Tourani et al. 2016). Notably, we opt for explicit parameters over additional MLPs to enhance optimization speed.

Concurrent work DP-NeRF (Lee et al. 2023) adopts a similar approach to our per-frame intrinsic refinement module by constraining deformable kernels from Deblur-NeRF to account for physical camera motion and the image acquisition process. However, DP-NeRF utilizes a complex series of MLPs with adaptive weights and focuses exclusively on deblurring color images. In contrast, our per-frame intrinsic refinement module focuses on refining intrinsic matrices to handle distortions in depth frames, utilizing a simple yet efficient formulation.

Method

In this section, we propose a neural RGB-D surface reconstruction method that integrates per-frame intrinsic refinement and TSDF Fusion-guided pretraining schemes for high-fidelity results (Fig. 1). Building upon the rendering scheme and objective functions proposed in (Azinović et al. 2022), we employ a dense feature grid similar to DVGO (Sun, Sun, and Chen 2021) and GO-Surf (Wang, Bleja, and Agapito 2022) to further enhance optimization speed. During ray casting, the per-frame intrinsic refinement

module refines the intrinsic matrix for each frame, effectively addressing inaccuracies caused by camera motion. To efficiently optimize our model, we adopt a three-phase training process, utilizing the TSDF Fusion algorithm and progressive learning technique. This enables us to achieve improved results with reduced computational burden.

Hybrid geometry representation

We use a dense feature grid to explicitly learn local features, reducing computational complexity and training time compared to an MLP. We dynamically build the feature grid per scene:

$$V^{(feat)} : (N_x \times N_y \times N_z) \mapsto \mathbb{R}^F, \quad (1)$$

where F is a fixed hyperparameter for feature vector length and N_x, N_y, N_z are the feature grid dimensions varied according to the scene size. We use the depth frames and the estimated camera poses to calculate the minimum bounding box size of the scene— L_x, L_y, L_z . With the grid cell size gs , each of N_x, N_y, N_z is set to $\lceil L_x/gs \rceil, \lceil L_y/gs \rceil, \lceil L_z/gs \rceil$ respectively. The feature vector ϕ_p for a 3D point p is simply the trilinear interpolation of the feature vectors of the nearest 8 grid vertices P_{near} .

$$\phi_p = \text{interp}[V^{(feat)}(P_{near})] \in \mathbb{R}^F \quad (2)$$

With the dense grid representation efficiently encoding local geometric features, we use shallow MLPs to decode the features into view-dependant color $C_{p,d}^i$ and truncated signed distance value \hat{D}_p of a 3D point p . In order to decode the view-dependant color information, positional-encoded ray direction d as in (Mildenhall et al. 2020) and frame-dependent latent embedding vector ξ introduced in (Martin-Brualla et al. 2021; Azinović et al. 2022) are concatenated with the feature vector before inputting to the color MLP. As described in Eqs. (3) and (4), two separate MLPs were used for color and signed distance value, respectively.

$$C_{p,d}^i = \text{MLP}^C(\phi_p, \Lambda(d), \xi_i), \quad (3)$$

$$\hat{D}_p = \text{MLP}^D(\phi_p), \quad (4)$$

where i is the frame number and Λ is the frequency positional encoding function.

The neural rendering process is designed in a similar way as in (Azinović et al. 2022). Given a known camera intrinsic matrix, the camera ray r for an image pixel (u, v) in normalized image plane is cast along its casting direction d :

$$d_{u,v} = [R \mid t] \begin{bmatrix} \varrho_{u,v} \\ 1 \end{bmatrix} \quad (5)$$

$$\varrho_{u,v} = \begin{bmatrix} 1/f_x & 0 & -c_x/f_x \\ 0 & -1/f_y & c_y/f_y \\ 0 & 0 & -1 \end{bmatrix} \begin{bmatrix} u \\ v \\ 1 \end{bmatrix} \quad (6)$$

where $[R \mid t]$ is the estimated camera pose matrix, f_x, f_y are focal lengths and (c_x, c_y) is the principal point. For a 3D point p , its weight value ω_p for rendering the color image is calculated from the signed distance value:

$$\omega_p = \sigma(\frac{\hat{D}_p}{tr}) \cdot \sigma(-\frac{\hat{D}_p}{tr}), \quad (7)$$

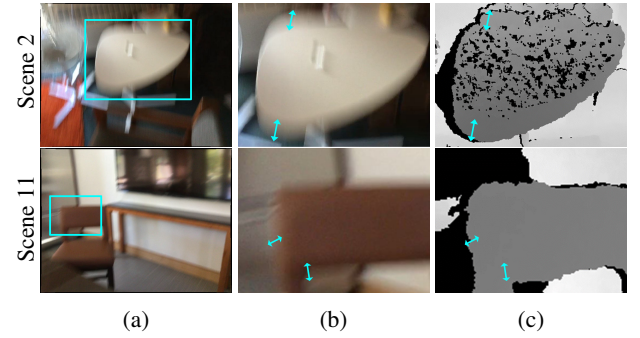


Figure 2: Samples from the ScanNet V2 (Dai et al. 2017) dataset demonstrate the negative impact of motion blurs. The RGB frames (a, b) are blurry and distorted. Unlike the color frames, the depth frames (c) contain extended object boundary rather than averaging blur (Tourani et al. 2016).

where tr is the truncation distance and σ is sigmoid function. Finally, the rendered color \hat{C} for a ray r with direction d of the i^{th} frame is the weighted sum of the radiance values on the sampled points p along the ray:

$$\hat{C}_r = \frac{1}{\sum \omega_p} \sum \omega_p C_{p,d}^i \quad (8)$$

Per-frame intrinsic refinement

In contrast to still images, video frames are susceptible to camera motion, resulting in motion blurs as depicted in Fig. 2. While motion blurs in color frames are typically modeled as averaging pixels over exposure time, motion blurs in depth frames act more like a min-filter, taking the minimum value during exposure time. This phenomenon can cause the boundaries to extend beyond actual object boundaries (Tourani et al. 2016). Our method is designed to handle motion blur in depth frames by correcting the camera intrinsic matrix, which effectively changes the scale and translation of the projected image plane.

Before handling this per-frame intrinsic refinement issue, we first adopt the image-plane deformation field and pose optimization techniques from (Azinović et al. 2022) to correct the camera-pose errors and the potential global errors from the intrinsic parameters as well as the camera lens distortion. We modify the image-plane deformation field to use a two-layered shallow MLP to reduce the training time.

Our per-frame intrinsic refinement scheme is performed after the image-plane deformation field has been applied to correct the depth-specific motion blurs. Specifically, we introduce four parameters per frame, two for scaling and the other two for translation purposes. Scaling and translation are applied to the normalized image coordinate before it is transformed into the world coordinate:

$$\hat{\varrho}_{u,v}^i = \mathbf{s}^i \cdot (\varrho_{u,v} + \tau^i) \quad (9)$$

$$\mathbf{s}^i = \begin{bmatrix} s_x^i & 0 & 0 \\ 0 & s_y^i & 0 \\ 0 & 0 & 1 \end{bmatrix}, \quad \tau^i = \begin{bmatrix} \tau_x^i \\ \tau_y^i \\ 0 \end{bmatrix} \quad (10)$$

where s^i and τ^i are trainable parameters for i^{th} frame and optimized during training. Accordingly, the refined casting direction $\hat{\mathbf{d}}$ is calculated from $\hat{\varrho}$:

$$\hat{\mathbf{d}}_{u,v}^i = [R \mid t] \begin{bmatrix} \hat{\varrho}_{u,v}^i \\ 1 \end{bmatrix} \quad (11)$$

Eq. (11) replaces Eq. (5) for generating rays and sampling points. These parameters can be interpreted as correcting the principal point and focal lengths of the intrinsic matrix. The image-plane deformation field and per-frame intrinsic refinement schemes both aim to refine ray directions to handle inaccuracies. While image-plane deformation field emphasizes global refinement, applied uniformly across all frames, per-frame intrinsic refinement focuses on handling frame-specific fluctuations that image-plane deformation field does not address.

Optimization

InFusionSurf is optimized through a three-phase training process as depicted in Fig. 1. In the first phase, InFusionSurf learns a geometric prior using the classical real-time algorithm, TSDF Fusion (Curless and Levoy 1996). Specifically, InFusionSurf builds a dense grid as in Eq. (1) with $F=1$ and runs TSDF Fusion with depth frames of the identical scene. We randomly sample grid cells, query the center points, and compare them with the corresponding points from the results of TSDF Fusion using mean squared error:

$$\mathcal{L}_{pre} = \frac{1}{|\mathbf{P}_b|} \sum_{\mathbf{p} \in \mathbf{P}_b} (\hat{D}_{\mathbf{p}} - D_{\mathbf{p}}^f)^2, \quad (12)$$

where \mathbf{P}_b is the set of sampled center points and $D_{\mathbf{p}}^f$ is the signed distance value from the TSDF Fusion result. Only $V^{(feat)}$ and MLP^D are trained during this phase, while the other parameters are fixed at their initial values. Leveraging TSDF Fusion as prior knowledge allows direct learning of signed distance values for 3D coordinates, eliminating the need for the time-consuming rendering process. This leads to a significant acceleration in the initial training phase.

For the second and third phases, InFusionSurf adopts the progressive learning technique (Sun, Sun, and Chen 2021; Yu et al. 2021) to successively learn low- and high-frequency details focusing on refining the geometric prior. All the parameters including those that were fixed during the first phase are optimized during these phases.

During the second phase, InFusionSurf is trained with randomly sampled ray batch r_b from the input frames. Inspired by (Azinović et al. 2022), we sample points S_c from the rays for every 15.625mm within the ray length where the ray length is varied depending on the scene, ranging from 4m to 10m, to cover the entire scene. Using the estimated signed distance values for each sampled point and the rendered color value as described in Eqs. (4) and (8), our loss function is defined similarly to (Azinović et al. 2022):

$$\mathcal{L} = \lambda_{fs} \mathcal{L}_{fs} + \lambda_{sdf} \mathcal{L}_{sdf} + \lambda_{rgb} \mathcal{L}_{rgb} + \lambda_{reg} \mathcal{L}_{reg} \quad (13)$$

\mathcal{L}_{fs} denotes the ‘free space’ loss that forces the sample points $\mathbf{p} \in S_{fs} \subset S_c$ that lie outside the truncated area

to have the signed distance value of tr :

$$\mathcal{L}_{fs} = \frac{1}{|r_b|} \sum_{r \in r_b} \frac{1}{|S_{fs}|} \sum_{\mathbf{p} \in S_{fs}} (\hat{D}_{\mathbf{p}} - tr)^2 \quad (14)$$

\mathcal{L}_{sdf} compares the predicted signed distance value of the sample points $\mathbf{p} \in S_{sdf} \subset S_c$ lying within the truncated area against $D_{\mathbf{p}}^i$, the signed distance value observed in the depth frame:

$$\mathcal{L}_{sdf} = \frac{1}{|r_b|} \sum_{r \in r_b} \frac{1}{|S_{sdf}|} \sum_{\mathbf{p} \in S_{sdf}} (\hat{D}_{\mathbf{p}} - D_{\mathbf{p}}^i)^2 \quad (15)$$

\mathcal{L}_{rgb} measures the difference between the predicted rendered color of the rays and the observed color of the corresponding pixels:

$$\mathcal{L}_{rgb} = \frac{1}{|r_b|} \sum_{r \in r_b} (\hat{C}_{\mathbf{p}}^i - C_{u,v}^i)^2 \quad (16)$$

\mathcal{L}_{reg} is the regularization term and consists of three parts:

$$\mathcal{L}_{reg} = \mathcal{R}_{embed} + \mathcal{R}_{refine} + \mathcal{R}_{deform}, \quad (17)$$

$$\mathcal{R}_{embed} = \frac{1}{|\nu|} \sum_{\nu_i \in \nu} \xi_{\nu_i}^2,$$

$$\mathcal{R}_{refine} = \frac{1}{|r_b|} \sum_{r \in r_b} ((s_r - 1)^2 + \tau_r^2),$$

$$\mathcal{R}_{deform} = \frac{1}{|r_b|} \sum_{r \in r_b} w_{ipdf}^2$$

where ξ_{ν_i} is the frame-dependent embedding vector for the frame ν_i within the input frame set ν , w_{ipdf} denote the MLP weights for the image-plane deformation field network, s_r and τ_r denote the transform parameters of the frame to which the ray r belongs, and $|\cdot|^2$ denotes element-wise squared sum operation.

InFusionSurf learns the fine details during the third phase, in which the dense feature grid is divided into higher resolutions so that the feature grid dimensions N_x, N_y, N_z become $\lceil L_x/(gs/2) \rceil, \lceil L_y/(gs/2) \rceil, \lceil L_z/(gs/2) \rceil$ respectively. We sample additional points S_f in small neighborhoods around the surfaces discovered from the previously sampled set of points S_c . The third phase is trained with the same loss function, Eq. (13), using both S_c and S_f .

Implementation details

We implemented our network with PyTorch, and the network was optimized using the ADAM optimizer (Kingma and Ba 2015) with 5×10^{-4} for learning rate, 0.9 for beta1, and 0.999 for beta2. The learning rate was set to exponentially decay so that it was decreased to a tenth for every 250K iterations. For the feature grid, we chose $F=12$ and $gs=10\text{cm}$, with weights initialized at 0. The signed distance values were truncated to $tr=5\text{cm}$. The MLP networks for the color and truncated signed distance values both consisted of 2 hidden layers with 128 nodes each. The MLP for the image-plane deformation field was built with 2 hidden layers with 64 nodes each. Per-frame intrinsic refinement optimization parameters were initialized to 1 for scaling and 0

for translation. The λ weights for the loss terms were set to 10 for λ_{fs} , 6×10^3 for λ_{sdf} , 0.5 for λ_{rgb} , and 0.1 for λ_{reg} . We ran 3K, 7K, and 65K iterations for each training phase, respectively. We used a CUDA implementation of the TSDF Fusion algorithm that can process, on average, 231.7 frames per second on Tesla V100 GPU (Zeng et al. 2017).

Experiments

We demonstrate comparative studies of InFusionSurf against prior work as well as an ablation study of the proposed framework components. Additionally, we present visualizations of the refined depth images to show the impact of the per-frame intrinsic refinement scheme.

For the evaluation of each study, we extracted the truncated signed distance values in 1cm^3 resolution and ran MarchingCubes (Lorensen and Cline 1987) algorithm to get the triangular meshes.

Datasets

We used ScanNet V2 (Dai et al. 2017) as a real-scene dataset during the qualitative study. The dataset used the rolling shutter method during image capture, resulting in motion blur, distortions, and noisy depth values, including holes and missing objects.

To compare quantitative results against the baseline methods, we used 10 synthetic scenes from (Azinović et al. 2022). They used indoor 3D models to photo-realistically render color and depth frames with ground truth camera trajectories. Depth frames were simulated with Kinect-like noises including holes and quantization noises.

Baselines

We compare our results with Neural RGB-D (Azinović et al. 2022) and GO-Surf (Wang, Bleja, and Agapito 2022). Specifically, we report our results at 20K and 75K iterations to respectively compare against GO-Surf and Neural RGB-D to show that InFusionSurf outperforms in terms of both efficiency and performance. We trained GO-Surf and Neural RGB-D with the hyperparameters recommended by the respective papers on a Tesla V100 GPU.

Results and discussion

Qualitative results The qualitative results are illustrated in Fig. 3. For the comparison with GO-Surf, our reconstruction results after 20K iterations is shown. As depicted in Fig. 3, InFusionSurf exhibits finer details and fewer erroneous surfaces throughout the scenes, even with a shorter training time.

After 75K iterations, our reconstruction qualities showed better results than Neural RGB-D, recovering the structures Neural RGB-D missed in some cases. Compared to Neural RGB-D, our training speed was 7.3 to 8.7 times faster.

Quantitative results We compared our method with baselines in terms of Chamfer ℓ_1 distance (C- ℓ_1), intersection-over-union (IoU), normal consistency (NC), and F-score. In order to compute C- ℓ_1 , NC, and F-score, we sampled point clouds from the output meshes in 1cm^2 resolution. We used

a threshold of 5cm for F-score. The evaluation meshes were voxelized with an edge length of 10cm to compute the IoU. As shown in Table 1, our result after 20K iterations outperforms GO-Surf in C- ℓ_1 , IoU, and F-score with less training time (20% faster on average). In the comparison with Neural RGB-D, Our method also showed superior C- ℓ_1 , IoU, and F-score. At the same time, it took 96 minutes on average to train 75K iterations, which was 7 times faster than what Neural RGB-D took. While InFusionSurf showed outstanding performance on the three major measures, it was less effective on the normal consistency, indicating that its results contained relatively uneven surfaces. The quantitative metrics imply that our method is best suited for quickly reconstructing complex geometries, rather than simple flat surfaces.

Ablation study The ablation study shows the effects of per-frame intrinsic refinement and TSDF Fusion-guided training phase. In order to qualitatively evaluate, we compared results at the same iteration points without the per-frame intrinsic refinement or the first phase of training—TSDF Fusion prior learning (Fig. 4). To quantitatively evaluate the effectiveness of the TSDF Fusion, we conducted a quantitative study with and without the TSDF Fusion-guided training phase (Table 1).

Moreover, we performed a comprehensive study to evaluate the effectiveness of the per-frame intrinsic refinement using simulated errors in the intrinsic matrix on a synthetic dataset. To achieve this, we deliberately initialized the focal length to 570 instead of its ground truth value, which is 554.26. Additionally, we introduced random fluctuations following a normal distribution $\mathcal{N}(0, 10^2)$ in both the focal length and the principal points per frame. We then optimized our model, considering different scenarios by omitting either one or both of the per-frame intrinsic refinement and image plane deformation field (Table 2).

As shown in Fig. 4, our per-frame intrinsic refinement method fixes the erroneous parts of the objects. The quantitative result represented in Table 2 implies that the image-plane deformation field and the per-frame intrinsic refinement impact complementarily on improving the quality of reconstructions. Our method adds only four additional parameters per frame, which can be optimized in the early stages of training. This effectively fixes reconstruction errors in small iterations, increasing the training time by just 2.7% on average.

As illustrated in Fig. 4, the TSDF Fusion prior learning phase consistently improves object reconstruction details across all scenes. Moreover, the lack of TSDF Fusion prior learning results in several minutes of added training time for the same iteration. This consistent pattern is further supported by the results presented in Table 1, where our approach excels in C- ℓ_1 , NC, and F-score metrics. The first phase of our training process, leveraging prior knowledge, is extremely fast because it directly learns the signed distance values of 3D coordinates instead of requiring the time-consuming rendering process, albeit with some inaccuracies. The subsequent training phases can dedicate their efforts to refining intricate details within the scene, ultimately

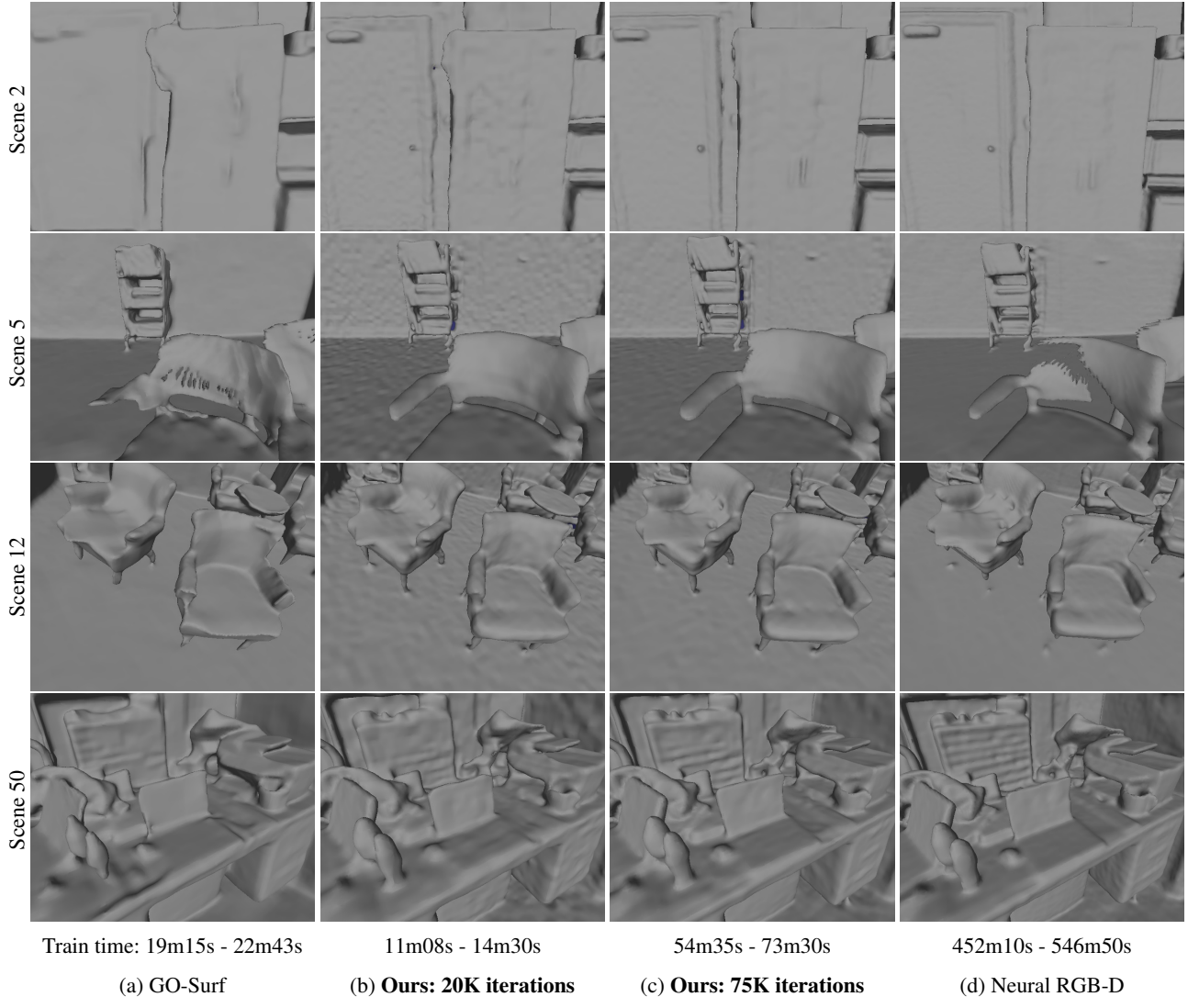


Figure 3: We compare our method with GO-Surf (Wang, Bleja, and Agapito 2022) and Neural RGB-D (Azinović et al. 2022) at different points in time. The comparison was conducted using scenes 2, 5, 12, and 50 from ScanNet V2 (Dai et al. 2017). When trained for a shorter amount of time, InFusionSurf-20K (b) recovers high-frequency details overlooked by GO-Surf (a) and generates much less erroneous surfaces. Given a longer training time, InFusionSurf-75K (c) achieves greater quality while recovering a number of geometries missing from Neural RGB-D (d).

Method	$C\ell_1 \downarrow$	IoU \uparrow	NC \uparrow	F-Score \uparrow	Time
GO-Surf	0.042	0.723	0.922	0.918	22m57s
Neural RGB-D	0.052	<u>0.757</u>	0.922	<u>0.938</u>	669m59s
Ours (20K)	0.038	0.737	0.904	0.929	18m24s
Ours (20K, w/o TSDF)	0.042	0.750	0.902	0.926	21m05s
Ours (75K)	<u>0.041</u>	0.768	<u>0.913</u>	0.939	95m57s

Table 1: Quantitative results on the synthetic scene dataset. InFusionSurf shows better $C\ell_1$, IoU, and F-score than GO-Surf (Wang, Bleja, and Agapito 2022) when trained for a shorter amount of time. After training for more iterations, it achieves better performances than Neural RGB-D (Azinović et al. 2022) with significantly less training time. The performance 20K iterations without TSDF Fusion (TSDF) implies that our TSDF Fusion-guided training phase improves both reconstruction qualities and training time.

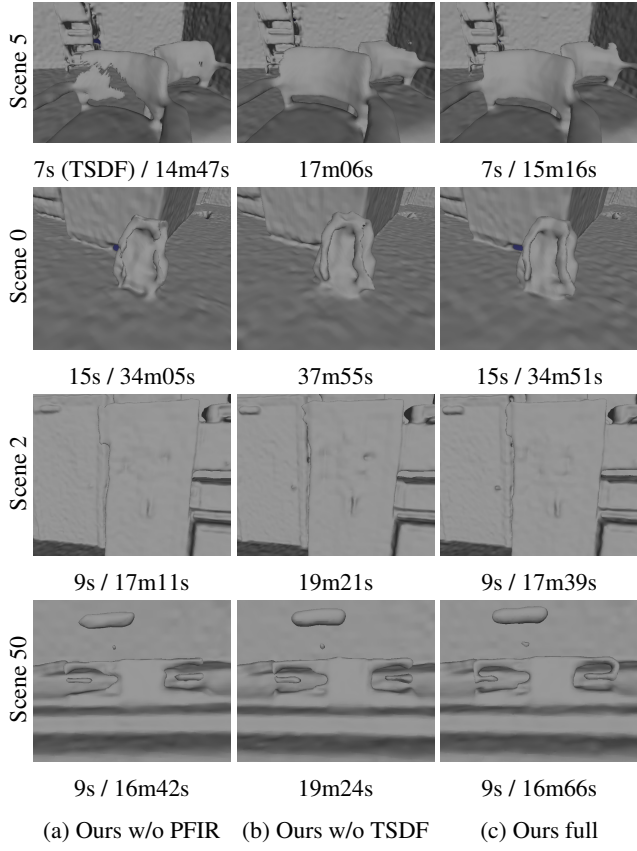


Figure 4: Ablation study. (a) Ours without per-frame intrinsic refinement (PFIR). (b) Ours without TSDF Fusion prior learning in the first phase of training (TSDF). (c) Ours with both methods applied. Timestamps below the subfigures represent the TSDF Fusion prior learning time (if applicable) and the total training time.

improving reconstruction quality while requiring less time to converge.

Visualization of intrinsic refined depth frame To evaluate the refinement results of our per-frame intrinsic refinement module, we performed experiments using depth frames from the ScanNet V2 dataset. For each frame, we transformed all pixels to image coordinates using the original intrinsic matrix, applied the scaling and translation and then re-projected them into pixels using the original intrinsic matrix. As shown in Fig. 5, the results clearly demonstrate the effectiveness of our per-frame intrinsic refinement module in recovering object boundaries within the depth frames. By compensating for errors caused by camera motion, our approach achieves more accurate reconstruction.

Limitation

A main limitation of our approach is the use of simple translation and scaling transformation matrices, primarily designed to correct motion blurs arising from camera movements. While effective in correcting distortions that uniformly affect the entire frames, this approach does not han-

PFIR	IDPF	$C\ell_1 \downarrow$	$\text{IoU} \uparrow$	$\text{NC} \uparrow$	$\text{F-Score} \uparrow$
		0.081	0.364	0.845	0.514
✓		0.067	0.486	0.861	0.645
✓		0.060	0.579	0.883	0.795
✓	✓	0.051	0.656	0.888	0.863

Table 2: Ablation study for the per-frame intrinsic refinement (PFIR) and image-plane deformation field (IPDF) on the quantitative dataset. Our PFIR and IPDF schemes demonstrate complementary impact on reconstruction quality.

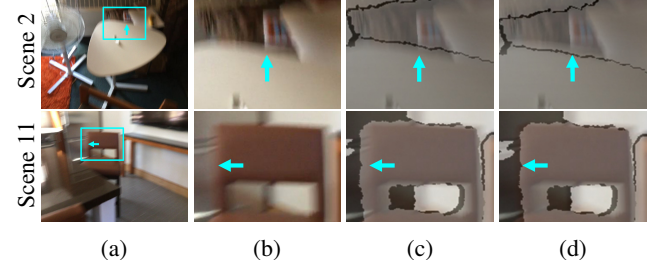


Figure 5: Visualization of our per-frame intrinsic refinement module. (a), (b) Color frames with camera motion blur. (c) Superimposed depth frames show incorrectly extended object boundaries. (d) Our per-frame intrinsic refinement module aligns the depth frames with the actual boundaries.

ble object motion blurs or rolling shutter effects, which occur locally around moving objects. Adopting advanced modeling techniques for the per-frame intrinsic refinement module could potentially improve accuracy by addressing unhandled distortion types. However, such advancements might come at the cost of reduced processing speed. Striking a balance between speed and accuracy is crucial in real-time or interactive applications, where faster processing times are often a priority. Future research could explore trade-offs and optimization strategies to enhance both accuracy and speed in the context of per-frame intrinsic refinement modeling.

Regarding evaluation, we used the ScanNet dataset which primarily consists of diffuse objects, since our focus was on reconstructing opaque surfaces. For the future, extending the framework to handle transparent or reflective surfaces could be a promising research direction.

Conclusion

In this paper, we introduced InFusionSurf, a NeRF-style RGB-D 3D reconstruction framework that leverages per-frame intrinsic refinement and TSDF Fusion to enhance reconstruction quality with minimal impact on optimization time. The comprehensive comparative evaluations showed that our method is capable of accurately reconstructing a scene with high-frequency details. We also demonstrated the effectiveness of the per-frame intrinsic refinement and TSDF Fusion prior learning techniques in the ablation study.

References

Azinović, D.; Martin-Brualla, R.; Goldman, D. B.; Nießner, M.; and Thies, J. 2022. Neural RGB-D Surface Reconstruction. In *Proceedings of the IEEE/CVF Conference on Computer Vision and Pattern Recognition (CVPR)*, 6290–6301.

Chen, A.; Xu, Z.; Zhao, F.; Zhang, X.; Xiang, F.; Yu, J.; and Su, H. 2021. MVSNeRF: Fast Generalizable Radiance Field Reconstruction from Multi-View Stereo.

Chen, Z.; and Zhang, H. 2018. Learning Implicit Fields for Generative Shape Modeling.

Curless, B.; and Levoy, M. 1996. A Volumetric Method for Building Complex Models from Range Images. In *Proceedings of the 23rd Annual Conference on Computer Graphics and Interactive Techniques, SIGGRAPH '96*, 303–312. New York, NY, USA: Association for Computing Machinery. ISBN 0897917464.

Dai, A.; Chang, A. X.; Savva, M.; Halber, M.; Funkhouser, T.; and Nießner, M. 2017. ScanNet: Richly-annotated 3D Reconstructions of Indoor Scenes. In *Proc. Computer Vision and Pattern Recognition (CVPR), IEEE*.

Dai, A.; Nießner, M.; Zollhöfer, M.; Izadi, S.; and Theobalt, C. 2016. BundleFusion: Real-time Globally Consistent 3D Reconstruction using On-the-fly Surface Re-integration.

Deng, K.; Liu, A.; Zhu, J.-Y.; and Ramanan, D. 2021. Depth-supervised NeRF: Fewer Views and Faster Training for Free.

Kingma, D. P.; and Ba, J. 2015. Adam: A Method for Stochastic Optimization. In Bengio, Y.; and LeCun, Y., eds., *3rd International Conference on Learning Representations, ICLR 2015, San Diego, CA, USA, May 7-9, 2015, Conference Track Proceedings*.

Kupyn, O.; Budzan, V.; Mykhailych, M.; Mishkin, D.; and Matas, J. 2018. DeblurGAN: Blind Motion Deblurring Using Conditional Adversarial Networks. arXiv:1711.07064.

Kupyn, O.; Martyniuk, T.; Wu, J.; and Wang, Z. 2019. DeblurGAN-v2: Deblurring (Orders-of-Magnitude) Faster and Better. arXiv:1908.03826.

Lee, D.; Lee, M.; Shin, C.; and Lee, S. 2023. DP-NeRF: Deblurred Neural Radiance Field with Physical Scene Priors. arXiv:2211.12046.

Lorensen, W. E.; and Cline, H. E. 1987. Marching Cubes: A High Resolution 3D Surface Construction Algorithm. In *Proceedings of the 14th Annual Conference on Computer Graphics and Interactive Techniques, SIGGRAPH '87*, 163–169. New York, NY, USA: Association for Computing Machinery. ISBN 0897912276.

Ma, L.; Li, X.; Liao, J.; Zhang, Q.; Wang, X.; Wang, J.; and Sander, P. V. 2022. Deblur-NeRF: Neural Radiance Fields from Blurry Images. arXiv:2111.14292.

Martin-Brualla, R.; Radwan, N.; Sajjadi, M. S. M.; Barron, J. T.; Dosovitskiy, A.; and Duckworth, D. 2021. NeRF in the Wild: Neural Radiance Fields for Unconstrained Photo Collections. In *Proceedings of the IEEE/CVF Conference on Computer Vision and Pattern Recognition (CVPR)*, 7210–7219.

Mildenhall, B.; Srinivasan, P. P.; Tancik, M.; Barron, J. T.; Ramamoorthi, R.; and Ng, R. 2020. NeRF: Representing Scenes as Neural Radiance Fields for View Synthesis.

Müller, T.; Evans, A.; Schied, C.; and Keller, A. 2022. Instant Neural Graphics Primitives with a Multiresolution Hash Encoding. *ACM Trans. Graph.*, 41(4): 102:1–102:15.

Nah, S.; Kim, T. H.; and Lee, K. M. 2018. Deep Multi-scale Convolutional Neural Network for Dynamic Scene Deblurring. arXiv:1612.02177.

Neff, T.; Stadlbauer, P.; Parger, M.; Kurz, A.; Mueller, J. H.; Chaitanya, C. R. A.; Kaplanyan, A.; and Steinberger, M. 2021. DONeRF: Towards Real-Time Rendering of Compact Neural Radiance Fields using Depth Oracle Networks. *Computer Graphics Forum*, 40(4): 45–59.

Newcombe, R. A.; Izadi, S.; Hilliges, O.; Molyneaux, D.; Kim, D.; Davison, A. J.; Kohi, P.; Shotton, J.; Hodges, S.; and Fitzgibbon, A. 2011. KinectFusion: Real-time dense surface mapping and tracking. In *2011 10th IEEE International Symposium on Mixed and Augmented Reality*, 127–136.

Nießner, M.; Zollhöfer, M.; Izadi, S.; and Stamminger, M. 2013. Real-Time 3D Reconstruction at Scale Using Voxel Hashing. *ACM Trans. Graph.*, 32(6).

Oechsle, M.; Peng, S.; and Geiger, A. 2021. UNISURF: Unifying Neural Implicit Surfaces and Radiance Fields for Multi-View Reconstruction.

Ortiz, J.; Clegg, A.; Dong, J.; Sucar, E.; Novotny, D.; Zollhoefer, M.; and Mukadam, M. 2022. iSDF: Real-Time Neural Signed Distance Fields for Robot Perception.

Peng, S.; Niemeyer, M.; Mescheder, L.; Pollefeys, M.; and Geiger, A. 2020. Convolutional Occupancy Networks.

Sucar, E.; Liu, S.; Ortiz, J.; and Davison, A. J. 2021. iMAP: Implicit Mapping and Positioning in Real-Time.

Sun, C.; Sun, M.; and Chen, H.-T. 2021. Direct Voxel Grid Optimization: Super-fast Convergence for Radiance Fields Reconstruction.

Sun, J.; Xie, Y.; Chen, L.; Zhou, X.; and Bao, H. 2021. NeuralRecon: Real-Time Coherent 3D Reconstruction from Monocular Video. In *2021 IEEE/CVF Conference on Computer Vision and Pattern Recognition (CVPR)*, 15593–15602. Los Alamitos, CA, USA: IEEE Computer Society.

Takikawa, T.; Litalien, J.; Yin, K.; Kreis, K.; Loop, C.; Nowrouzezahrai, D.; Jacobson, A.; McGuire, M.; and Fidler, S. 2021. Neural Geometric Level of Detail: Real-time Rendering with Implicit 3D Shapes.

Tao, X.; Gao, H.; Wang, Y.; Shen, X.; Wang, J.; and Jia, J. 2018. Scale-recurrent Network for Deep Image Deblurring. arXiv:1802.01770.

Tourani, S.; Mittal, S.; Nagariya, A.; Chari, V.; and Krishna, M. 2016. Rolling shutter and motion blur removal for depth cameras. In *2016 IEEE International Conference on Robotics and Automation (ICRA)*, 5098–5105.

Wang, J.; Bleja, T.; and Agapito, L. 2022. GO-Surf: Neural Feature Grid Optimization for Fast, High-Fidelity RGB-D Surface Reconstruction.

Wang, P.; Liu, L.; Liu, Y.; Theobalt, C.; Komura, T.; and Wang, W. 2021. NeuS: Learning Neural Implicit Surfaces by Volume Rendering for Multi-view Reconstruction.

Wang, R.; and Tao, D. 2014. Recent Progress in Image De-blurring. arXiv:1409.6838.

Wei, Y.; Liu, S.; Rao, Y.; Zhao, W.; Lu, J.; and Zhou, J. 2021. NerfingMVS: Guided Optimization of Neural Radiance Fields for Indoor Multi-view Stereo.

Yariv, L.; Kasten, Y.; Moran, D.; Galun, M.; Atzmon, M.; Basri, R.; and Lipman, Y. 2020. Multiview Neural Surface Reconstruction by Disentangling Geometry and Appearance.

Yu, A.; Fridovich-Keil, S.; Tancik, M.; Chen, Q.; Recht, B.; and Kanazawa, A. 2021. Plenoxels: Radiance Fields without Neural Networks.

Zamir, S. W.; Arora, A.; Khan, S.; Hayat, M.; Khan, F. S.; Yang, M.-H.; and Shao, L. 2021. Multi-Stage Progressive Image Restoration. arXiv:2102.02808.

Zeng, A.; Song, S.; Nießner, M.; Fisher, M.; Xiao, J.; and Funkhouser, T. 2017. 3DMatch: Learning Local Geometric Descriptors from RGB-D Reconstructions. In *CVPR*.

Zollhöfer, M.; Stotko, P.; Görilitz, A.; Theobalt, C.; Nießner, M.; Klein, R.; and Kolb, A. 2018. State of the Art on 3D Reconstruction with RGB-D Cameras. *Computer Graphics Forum*, 37: 625–652.